

Catch Missing Details: Image Reconstruction with Frequency Augmented Variational Autoencoder

Xinmiao Lin
Rochester Institute of Technology
x13439@rit.edu

Yikang Li
OPPO US Research
yikang.li1@oppo.com

Jenhao Hsiao
OPPO US Research
mark@oppo.com

Chiuman Ho
OPPO US Research
chiuman@oppo.com

Yu Kong
Michigan State University
yukong@msu.edu

Abstract

The popular VQ-VAE models reconstruct images through learning a discrete codebook but suffer from a significant issue in the rapid quality degradation of image reconstruction as the compression rate rises. One major reason is that a higher compression rate induces more loss of visual signals on the higher frequency spectrum which reflect the details on pixel space. In this paper, a Frequency Complement Module (FCM) architecture is proposed to capture the missing frequency information for enhancing reconstruction quality. The FCM can be easily incorporated into the VQ-VAE structure, and we refer to the new model as Frequency Augmented VAE (FA-VAE). In addition, a Dynamic Spectrum Loss (DSL) is introduced to guide the FCMs to balance between various frequencies dynamically for optimal reconstruction. FA-VAE is further extended to the text-to-image synthesis task, and a Cross-attention Autoregressive Transformer (CAT) is proposed to obtain more precise semantic attributes in texts. Extensive reconstruction experiments with different compression rates are conducted on several benchmark datasets, and the results demonstrate that the proposed FA-VAE is able to restore more faithfully the details compared to SOTA methods. CAT also shows improved generation quality with better image-text semantic alignment.

1. Introduction

VQ-VAE models [6, 11, 25, 29, 39, 46] reconstruct images through learning a discrete codebook of latent embeddings. They gained wide popularity due to the scalable and versatile codebook, which can be broadly applied to many visual tasks such as image synthesis [11, 49] and inpainting [4, 31]. A higher compression rate is typically preferable in VQ-

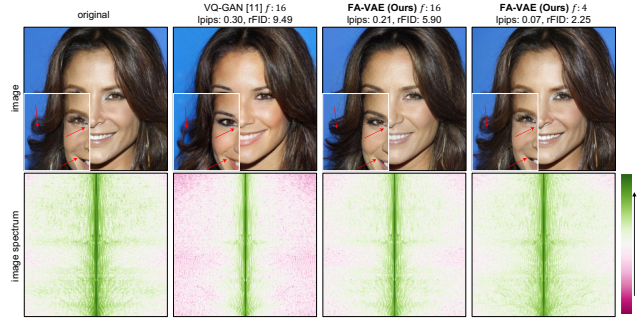


Figure 1. Images and their frequency maps. Row 1: original and reconstructed images. Row 2: the frequency maps of images, frequency increases in any direction away from the center. f is the compression rate. With a greater compression rate, more details are lost during reconstruction, i.e. eyes and mouth shape, and hair texture (pointed with red arrows) which align with the loss of high-frequency features. All frequency figures in this paper use the same colormap. rFID [14] and lpips [16] are lower the better, and frequency values increase from red to green, zoom in for better visualization.

VAE models since it provides memory efficiency and better learning of coherent semantics structures [11, 40].

One main challenge quickly arises for a higher compression rate, which severely compromises reconstruction accuracy. Figure 1 row 1 shows that although the reconstructed images at higher compression rates appear consistent with the original image, details inconsistencies such as the color and contour of the lips become apparent upon closer scrutiny. Figure 1 row 2 reveals that similar degradation also manifests on the frequency domains where features towards the middle and higher frequency spectrum are the least recoverable with greater compression rate.

Several causes stand behind this gap between pixel and frequency space. The convolutional nature of autoencoders is prone to *spectral bias*, which favors learning low-frequency features [22, 36]. This challenge is further ag-

gravated when current methods exclusively design losses or improve model architecture for better semantics resemblance [11,16,25] but often neglect the alignment on the frequency domain [12,15]. On top of that, it is intuitively more challenging for a decoder to reconstruct an image patch from a single codebook embedding (high compression) than multiple embeddings (less compression). The reason is that the former mixes up features of incomplete and diverse frequencies, while the latter could preserve more fine-grained and complete features at various frequencies.

Inspired by these insights, the *Frequency Augmented VAE (FA-VAE)* model is proposed, which aims to improve reconstruction quality by achieving better alignment on the frequency spectrums between the original and reconstructed images. More specifically, new modules named *Frequency Complement Modules (FCM)* are crafted and embedded at multiple layers of FA-VAE’s decoder to learn to complement the decoder’s features with missing frequencies.

We observe that valuable middle and high frequencies are mingled with the encoder’s feature maps during the compression via an encoder, shown in Figure 3 row 4. Therefore, a new loss termed *Spectrum Loss (SL)* is proposed to guide FCMs to generate missing features that align with the same level’s encoder features on the frequency domain. Since most image semantics reside on the low-frequency spectrum [48], SL prioritizes learning lower-frequency features with diminishing weights as frequencies increase.

Interestingly, we discover that checkerboard patterns appear in the complemented decoder’s features with SL, although better reconstruction performance is achieved (Figure 3 column 4). We speculate that because SL sets a deterministic range for the low-frequency spectrum when applying weights on the frequencies without considering that the importance of a frequency can vary from layer to layer. Thus, an improved loss function *Dynamic Spectrum Loss (DSL)* is crafted on top of SL with a learnable component to adjust the range of low-frequency spectrum dynamically for optimal reconstruction. DSL can improve reconstruction quality even further than SL without the unnatural checkerboard artifacts in the features (Figure 3 column 5).

We further extend FA-VAE to the text-to-image generation task and propose the *Cross-attention Autoregressive Transformer (CAT)* model. We first observe that only using one or a few token embeddings is a coarse representation of lengthy texts [8,27,33]. Thus CAT uses all token embeddings as a condition for more precise guidance. Moreover, existing works typically use self-attention, and the text condition is embedded merely at the beginning of the generation [11,49]. This mechanism becomes problematic in the autoregressive generation because one image token is generated at a time, thus the text condition gradually loosens its connection with the generated tokens. To circumvent this

issue, CAT embeds a cross-attention mechanism that allows the text condition to guide each step generation.

To summarize, our work includes the following contributions:

- We propose a new type of architecture called *Frequency Augmented VAE (FA-VAE)* for improving image reconstruction through achieving more accurate details reconstruction.
- We propose a new loss called *Spectrum Loss (SL)* and its enhanced version *Dynamic Spectrum Loss (DSL)*, which guides the *Frequency Complement Modules (FCM)* in FA-VAE to adaptively learn different low/high frequency mixtures for optimal reconstruction.
- We propose a new *Cross-attention Autoregressive Transformer (CAT)* for text-to-image generation using more fine-grained textual embeddings as a condition with a cross-attention mechanism for better image-text semantic alignment.

2. Related Work & Background

Image Reconstruction Vector Quantized-Variational AutoEncoder (VQ-VAE) [46] extends the Variational AutoEncoder structure [23] and proposes to encode images into discrete latent codes using vector quantization (VQ). Then a generative model, such as an autoregressive transformer [13], can be trained and paired with the decoder in VQ-VAE to synthesize new images. Later works [11,25,39] further improve the reconstruction and generation quality by improving the generative model architecture or the quantization efficiency. Since VQ-VAE models operate on discrete latent spaces, they cannot be directly and fairly compared to other VAE-based models that employ continuous latent space [1,6,23,29,45,51]. In contrast to current VQ-VAE models, our proposed FA-VAE technique improves reconstruction through the frequency angle and is more generalized since the FCMs can be readily extended to other neural networks that share the same VQ-VAE structure.

Few other works do image reconstruction via the frequency perspective. FFL [15] proposed a loss function to penalize differences on the hard frequencies. A new module, which is designed in the continuous latent space for image compression, is proposed to be incorporated into the encoder and decoder in [12]. To our best knowledge, FA-VAE is the first work that aims to improve image reconstruction on discrete latent space through the frequency perspective.

Image Generation Image generation can be achieved via GAN-based models [3,18,42,44,52,55], which synthesize images from noise vectors unconditionally or conditioned on different inputs such as texts, masks, etc. It becomes cumbersome to train one model for one application. Thus, StyleGAN [21] encodes semantic attributes into a continuous latent space, and subsequent works [19,20,

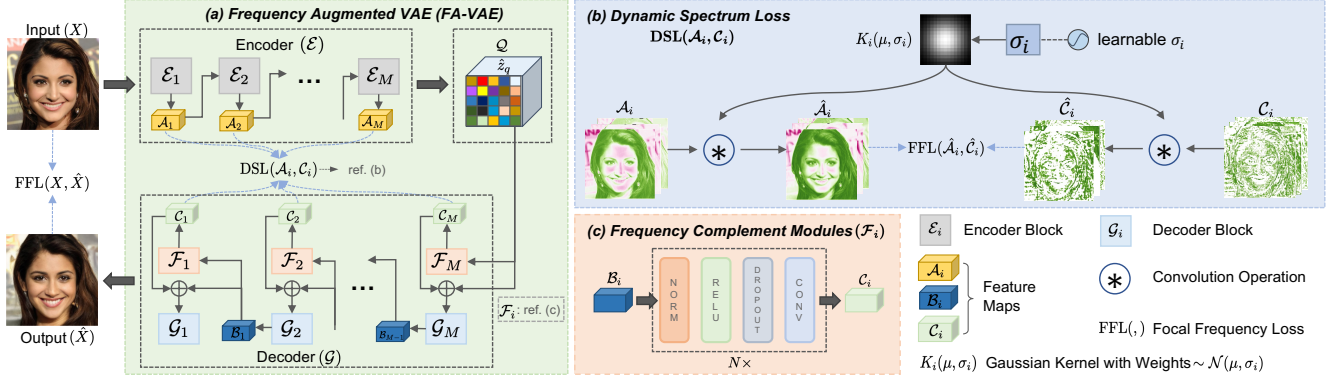


Figure 2. **Frequency Augmented VAE (FA-VAE)**. (a) The encoder \mathcal{E} encodes the images X onto discrete latent codebook space \hat{z}_q which is used by the decoder \mathcal{G} to reconstruct images \hat{X} . DSL (b) guides the FCMs (c) to learn to complement the reconstructed features with missing features of important frequencies in order to improve reconstruction quality. A more detailed figure is in the supplement.

[24, 32, 43, 50, 54] leverage this space for generating images conditioned on attributes or textual descriptions. However, StyleGAN-based models cannot scale to large datasets when the number of attributes becomes substantially large because this demands to increase model’s size. In contrast, the codebook in VQ-VAE models [46] is scalable to large datasets without additional model complexity. Diffusion-based models [5, 7, 10, 27, 28, 37, 40, 41] generate images from Gaussian noise through a reverse diffusion process can often require substantial training and large datasets. Most text-to-image generation models commonly use one of a few embeddings for a condition [8, 27, 38, 49] from pre-trained models such as CLIP [33] or T5-XXL [35]. In contrast, our proposed autoregressive transformer CAT uses the embeddings from all the text tokens for more fine-grained guidance during image generation.

VQ-VAE We now describe the VQ-VAE model [46] as it is the backbone used in the FA-VAE model, which is presented in Figure 2. VQ-VAE [46] and related models [11, 25, 38, 39] consist of an encoder that encodes the images into a codebook of embeddings. Then, a decoder is trained to reconstruct the images from a discrete set of codebook embeddings. In this paper, reconstruction loss in VQ-GAN is utilized which is:

$$\mathcal{L}_{rec} = \|X - \hat{X}\|_1 + \mathcal{L}_{pips}(X - \hat{X}) \quad (1)$$

where X and \hat{X} are the original and reconstructed images. We also use the adversarial setting of VQ-GAN model which introduced a discriminator compared to VQ-VAE models [39, 46], more details could be referred to [11].

3. Methodology

The proposed **Frequency Augmented VAE (FA-VAE)** is presented in Figure 2. In this section, we describe how FA-VAE ameliorates reconstruction quality by bridging the spectrum domain gap between reconstructed and original images. By explicitly embedding *Frequency Complement*

Modules (FCM) into the decoder, *Dynamic Spectrum Loss (DSL)* leverages important features frequency-wise from the encoder and guides the FCMs to complement the features of the decoder for better frequency restoration at different reconstruction stages.

3.1. Frequency Augmented VAE (FA-VAE)

Let the images be $X \in \mathbb{R}^{H \times W \times 3}$. The codebook \mathcal{C} is a set of $|\mathcal{C}|$ embeddings, such as $\mathcal{C} = \{\mathbf{c}_i | i = 1, \dots, |\mathcal{C}|\} \in \mathbb{R}^{n_z}$ and n_z is the length of one codebook embedding. FA-VAE consists of an encoder \mathcal{E} that encodes the images X into latent space representations such as $z = \mathcal{E}(x)$, for $z \in \mathbb{R}^{h \times w \times n_z}$ and $x \in X$, $(h \times w)$ is the resolution of the encoded representation. Let $f = H/h = W/w$ be the downsampling factor or compression rate. Each feature of z is approximated by the vector quantization block \mathcal{Q} using the nearest codebook entries, and it can be presented as:

$$\mathcal{Q}(z) = \hat{z}_q = \arg \min_{c_k \in \mathcal{C}} \|z_{ij} - \mathbf{c}_k\| \quad (2)$$

where \hat{z}_q is the quantized latent embedding and subsequently used by the decoder \mathcal{G} to produce the reconstructed image $\hat{x} = \mathcal{G}(\hat{z}_q)$.

3.1.1 Frequency Complement Modules (FCM)

Motivation Figure 1 shows that a higher compression rate leads to more significant reconstruction disparities on the higher-frequency spectrum. Existing models [11, 25, 39] guide the reconstructed images to be more aligned on the pixel and feature spaces with the original images (Eq. 1) but neglect frequency spectrum alignment and leave the encoder and decoder without further guidance. Figure 3 column 2 shows that the encoder activations \mathcal{A}_1 of baseline VQ-GAN [11] contain rich high-frequency features (row 3 & 4), but the decoder’s activations could mainly restore low-frequency features (row 5 & 6).

Therefore we propose *Frequency Complement Modules* (*FCM*), illustrated in Figure 2 (c), which aims to complement the decoder’s feature maps \mathcal{B}_i with features of missing frequencies using the encoder activations \mathcal{A}_i . The *FCMs* \mathcal{F}_i consist of sequences of convolution layers and activations. The decoder \mathcal{G} with *FCMs* embedded can be represented as:

$$\begin{aligned} \mathcal{B}_{M-1} &= \mathcal{G}_M (\mathcal{C}_M + \hat{z}_q) = \mathcal{G}_M (\mathcal{F}_M(\hat{z}_q) + \hat{z}_q) \\ &\dots \\ \mathcal{B}_1 &= \mathcal{G}_2(\mathcal{C}_2 + \mathcal{B}_2) = \mathcal{G}_2(\mathcal{F}_2(\mathcal{B}_2) + \mathcal{B}_2) \end{aligned} \quad (3)$$

Similarly, the encoder \mathcal{E} can be abstracted to:

$$z = \mathcal{E}(x) = \mathcal{E}_M (\dots (\mathcal{E}_2 (\mathcal{E}_1(x)))) \quad (4)$$

where \mathcal{G}_i is the i -th layer of the decoder, and $\mathcal{A}_i = \mathcal{E}_i(x)$ is the outputs or feature maps of the corresponding encoder block. The outputs of previous blocks \mathcal{B}_i are complemented by outputs $\mathcal{C}_i = \mathcal{F}_i(\mathcal{B}_{i+1})$, which contain the frequency-rich features learned from the encoder activations \mathcal{A}_i . The following section describes how Dynamic Frequency Loss (DSL) guides the learning of *FCMs* to specifically learn to complement \mathcal{B}_i with the features of missing frequencies.

In the paper, the frequency feature compensation is implemented by addition (in Eq. 3). However, the *FCM* is flexible in adopting any architecture and merging techniques, as illustrated by the three examples in Figure 5. Note that no architecture limitation is imposed on the encoder and decoder blocks as long as \mathcal{A}_i and \mathcal{B}_i share the same resolution. VQ-GAN [11] and related models [25, 46] already have similar architecture, and VQ-GAN is chosen as the backbone for FA-VAE.

3.1.2 Dynamic Spectrum Loss (DSL)

Motivation *Spectrum Loss (SL)* is proposed to guide explicitly the outputs of *FCMs* \mathcal{C}_i to be more aligned with the encoder’s activations \mathcal{A}_i on the frequency spectrum because the latter contains rich features on the higher frequency spectrum (Figure 3). Moreover, to account for the varying importance of frequencies across different decoder stages, *Dynamic Spectrum Loss (DSL)* is proposed, a more generalized variant of SL, and has the ability to adjust weights put on higher-frequency spectrum adaptively. Thus, each decoder block’s outputs can be enriched with features of the most critical frequencies for an accurate reconstruction.

Background The outputs \mathcal{A}_i of encoder block \mathcal{E}_i and \mathcal{C}_i of *FCM* block \mathcal{F}_i are first transformed to the frequency domain using Discrete Fourier Transform (DFT) as follows:

$$F(u, v) = \sum_{x=0}^{M-1} \sum_{y=0}^{N-1} f(x, y) \cdot e^{-i2\pi(\frac{ux}{M} + \frac{vy}{N})} \quad (5)$$

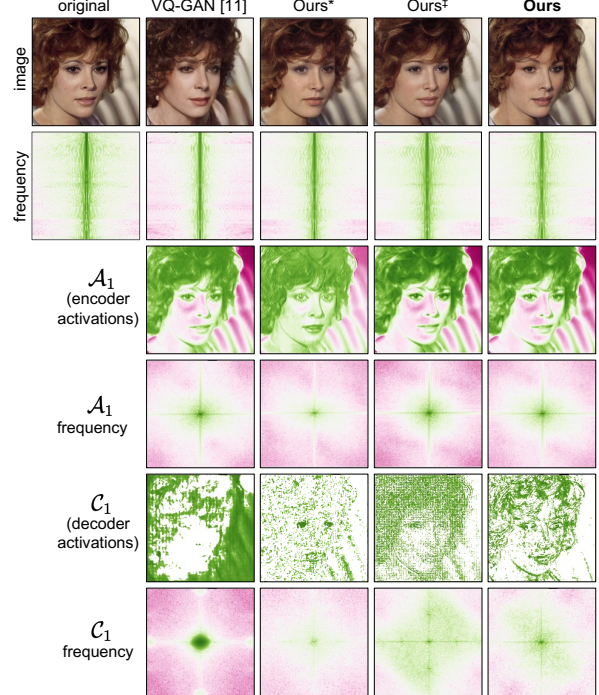


Figure 3. Image, activations, and their frequency maps. Ours* is FA-VAE model with FFL [15], Ours‡ is FA-VAE with SL and Ours is FA-VAE model with DSL. DSL shows a more harmonious balance between low- and high-frequencies (row 5) and more accurate reconstruction in mouth and hair textures. The frequency maps are plotted using the average of all channels and the contrast is adjusted to emphasize the higher frequency spectrums.

where e and i are Euler’s number and the imaginary unit. $M \times N$ is the spatial resolution of feature maps and the Fourier Transform (Eq. 5) is applied to each of them. $f(x, y)$ is the value at (x, y) of each feature map. $F(u, v)$ is the corresponding value at (u, v) coordinates on the frequency spectrum. The Focal Frequency Loss (FFL) [15] can be presented as:

$$\text{FFL}(\mathcal{A}_i, \mathcal{C}_i) = \frac{1}{MN|\mathcal{C}_i|} \sum_{c=0}^{|\mathcal{C}_i|-1} \sum_{u=0}^{M-1} \sum_{v=0}^{N-1} w(u, v) J(u, v), \quad (6)$$

where $w(u, v) = |F_{\mathcal{A}_i}(u, v) - F_{\mathcal{C}_i}(u, v)|$ are the weights put on each frequency. $J(u, v) = |F_{\mathcal{A}_i}(u, v) - F_{\mathcal{C}_i}(u, v)|^2$ is the main error function based on the frequency difference. The $|\mathcal{C}_i|$ is the number of feature maps in \mathcal{A}_i and \mathcal{C}_i . Both real and imaginary parts of the frequency domain are considered, more details are in [15].

Limitations of FFL Eq. 6 demonstrates that FFL puts modulating term $w(u, v)$ to focus learning on the hardest frequencies for reconstruction, which are the higher frequencies following our observation (Figures 1 & 3). However, this could not be ideal because features on the lower frequencies define the image content, and overemphasizing the higher frequencies could over-constrain the learning

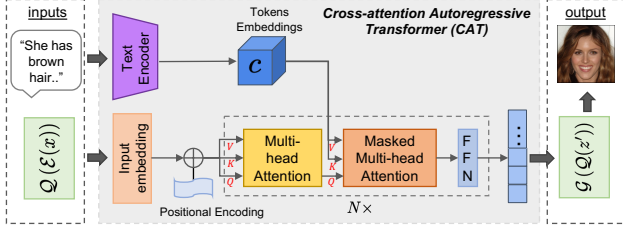


Figure 4. Cross-attention Autoregressive Transformer (CAT).

and lead to sub-optimal reconstruction, see Figure 7 row 1 column 3 and Table 2 row 3. Moreover, Figure 3 column 3 shows FCMs guided by a simple FFL can improve reconstruction performance (Ours*). However the frequency maps of the decoder activations \mathcal{C}_1 contain excessive noise due to overemphasis on the higher frequency spectrum, and lower frequencies are neglected (row 6).

Spectrum Loss (SL) Thus, we propose to apply a low-pass filter on the weights $w(u, v)$ in Eq. 6 to penalize more mismatch in the lower-frequency domain and gradually diminish the penalizing weights towards higher frequency spectrum. Therefore, let the Gaussian kernels be $K_i(\mu, \sigma)$ with weights initialized using mean and standard deviation (μ, σ_i) , and applied over the feature maps as:

$$(\hat{\mathcal{A}}_i, \hat{\mathcal{C}}_i) = (K_i(\mu, \sigma_i) \star \mathcal{A}_i, K_i(\mu, \sigma_i) \star \mathcal{C}_i). \quad (7)$$

where the \star is the convolution operation. Then, the *Spectrum Loss (SL)* is defined as:

$$\text{SL}(\mathcal{A}_i, \mathcal{C}_i) = \text{FFL}(\hat{\mathcal{A}}_i, \hat{\mathcal{C}}_i). \quad (8)$$

Limitations of SL Up until now, a fixed Gaussian filter $K_i(\mu, \sigma_i)$ is applied over all \mathcal{A}_i and \mathcal{C}_i of all encoder and decoder blocks. Figure 3 column 4 demonstrates that SL (Ours[‡]) improves reconstruction on the lower frequency spectrum, leading to better reconstruction than the baseline model (Table 2 row 5 vs row 1). However, checkerboard artifacts are also present (row 5) on \mathcal{C}_1 . One reason is that deterministic variance σ_i assumes that decoder activations across different levels require the same amount of higher frequency features for accurate reconstruction, which could be an over-rigid constraint on the learning. Another reason could be that the same σ_i magnifies the checkerboard effects produced by upsampling or striding operations in CNNs which are normally circumvented by subsequent convolutional layers [2, 30]. In the observation of the experiments, we find that the checkerboard effects can be intensified with the same σ_i in different layers due to the bounding effect between low frequency and high frequency (shown in Figure 3 column 4 row 6).

Dynamic Spectrum Loss (DSL) Therefore, we propose to optimize the variances σ_i instead of setting them as static hyperparameters to suit the different amounts of frequencies needed for each block's \mathcal{B}_i . The new *Dynamic Spectrum Loss (DSL)* is a more generalized form of Spectrum Loss

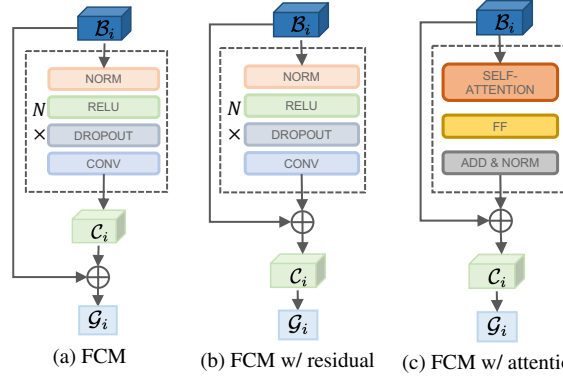


Figure 5. FCM with different architectures and connections.

(SL) with learnable σ_i . Note that DSL also includes FFL as a special form when used on the original and reconstructed images without the Gaussian filters.

Then the total reconstruction loss for FA-VAE can be described as:

$$\begin{aligned} \mathcal{L}_{rec} &= \alpha \text{FFL}(X, \hat{X}) + \beta \sum_{i=0}^{M-1} \text{DSL}(\mathcal{A}_i, \mathcal{C}_i) \\ &\quad + \|X - \hat{X}\|_1 + \mathcal{L}_{pips}(X - \hat{X}). \end{aligned} \quad (9)$$

where $\text{FFL}(X - \hat{X})$ is the Focal Frequency Loss applied on the original reconstructed images. The second term in Eq. 9 is the DSL loss applied over the outputs of the encoder and FCM blocks. The first two losses aim to minimize the frequency spectrum differences on the images and internal feature maps. The third and fourth losses act on the pixel and feature maps space [11]. α and β are hyperparameters.

σ_i are model parameters and optimized as:

$$\sigma_i^*, \mathcal{E}^*, \mathcal{G}^*, \mathcal{C}^* = \arg \min_{\sigma_i, \mathcal{E}, \mathcal{G}, \mathcal{C}} (\mathcal{L}_{rec} + \mathcal{L}_Q) \quad (10)$$

\mathcal{L}_Q is the quantization loss which minimizes the difference between the codebook embeddings and the embeddings given by the encoder \mathcal{E} , more details in [11]. We also use the L_2 regularization on the codebook embeddings during quantization as in [53] and exponential moving average (EMA) for updating the codebook [46] as they provide more stable training for the quantization block \mathcal{Q} .

Benefits of DSL The advantages of learnable σ_i in DSL are shown in Figure 3 column 5 where the reconstructed activations show no checkerboard artifacts as in column 4. Moreover, the reconstructed activations \mathcal{C}_1 are more similar to the encoder activations \mathcal{A}_1 on the frequency spectrum. Compared to the baseline model (column 2), our model exhibits a more harmonious balance between low- and high-frequencies, leading to more accurate reconstructed images.

3.2. Cross-attention Autoregressive Transformer (CAT)

We further extend FA-VAE to the text-to-image generation task and introduce a new *Cross-attention Autoregres-*

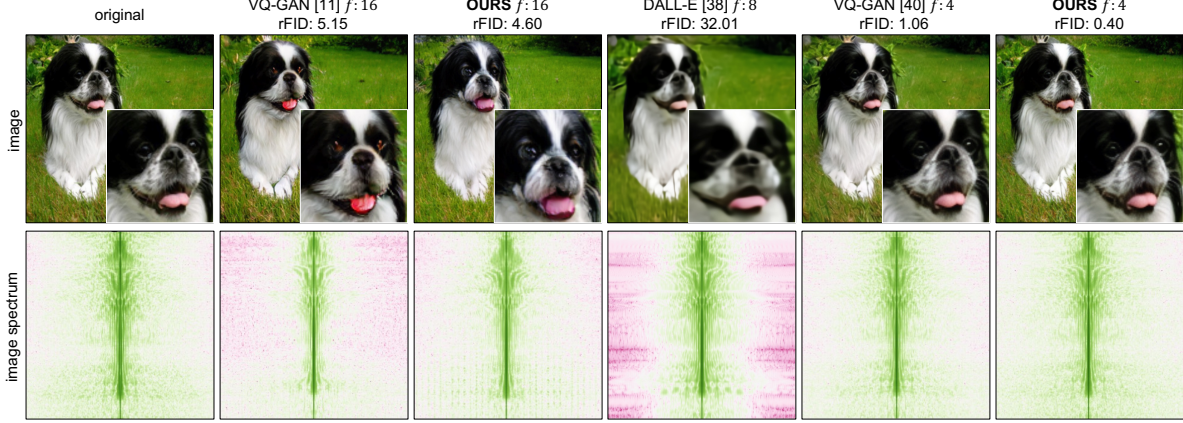


Figure 6. Reconstruction on ImageNet [9], label: Japanese terrier.

sive Transformer (CAT), presented in Figure 4. CAT uses all the token embeddings of a textual description given by the pretrained text encoder of CLIP model [33], while existing works mostly use one or partial textual embeddings [8, 38, 49]. Furthermore, CAT uses a cross-attention mechanism with the text tokens to guide the image generation at each step. This more fine-grained text condition allows the generation to capture more precisely the relationships of semantic attributes between text and image.

$$p(s|c) = \prod_i p(s_i|s_{<i}, c) \quad (11)$$

Then the predicted indices z' can be decoded to an image using FA-VAE’s decoder G . The loss is to maximize the log-likelihood of the data representations,

$$\mathcal{L}_{\text{CAT}} = \mathbb{E}_{x \sim p(x)}[-\log p(s)] \quad (12)$$

In this paper, the GPT2 model [34], which is the default setting in [11, 49], is utilized as the backbone for CAT, and cross-attention mechanism inspired from [47] is applied with the GPT2 structure.

4. Experiments

4.1. Experimental Details

The datasets used in this paper are: (1) Multi-Modal CelebA-HQ dataset [50] with 30,000 high-resolution celebrity face images and each image comes with ten captions; (2) Flickr-Faces-HQ (FFHQ) dataset [21] of 70,000 high-resolution face images; (3) ImageNet [9] that contains around 1 million images from 1000 categories. Experiments are performed on V-100 GPUs and results are reported on the validation sets unless specified otherwise. For a fair comparison with existing models, the resolutions used for training are 256×256 on all datasets. The details of training settings and hyperparameters are provided in the supplementary materials.

Model	Dataset	Codebook Size	$(h \times w)$	rFID \downarrow
RQ-VAE [25]	FFHQ	2048	(8×8)	5.33
FA-VAE (Ours)	FFHQ	2048	(16×16)	4.98
VQ-VAE-2 [39]	ImageNet	512	(64×64) & (32×32)	~ 10 (train)
VQ-GAN [40]	ImageNet	8192	(64×64)	1.06
FA-VAE (Ours)	ImageNet	8192	(64×64)	0.40
DALL-E [38]	ImageNet	8192	(32×32)	32.01
VQ-GAN [11]	ImageNet	16384	(16×16)	5.15
VQ-GAN [11]	ImageNet	1024	(16×16)	7.94
VQ-GAN [25]	ImageNet	16384	(8×8)	17.95
RQ-VAE [†] [46]	ImageNet	16384	(8×8)	10.77
RQ-VAE* [25]	ImageNet	16384	(8×8)	4.73
FA-VAE (Ours)	ImageNet	16384	(16×16)	4.60

Table 1. Reconstruction results on the validation data of FFHQ [21] and ImageNet [9] respectively, more results in the supplement. \dagger means depth 2, and $*$ means depth 4 from RQ-VAE [25].

4.2. Image Reconstruction

Reconstruction on FFHQ and Imagenet The experiment results of reconstruction on FFHQ [21] and ImageNet [9] are presented in Table 1. The results of the baselines are from the original paper. Note that smaller h and w means that the downsampling factor or the compression rate f is larger. FA-VAE model shows improved reconstruction quality over baseline models across different compression rates in both datasets. The main reason is that FA-VAE can successfully reconstruct the important middle and high-frequencies which are neglected in baseline models.

Figure 6 further supports our previous claim and demonstrates clear diverging reconstruction qualities between baseline models VQ-GAN [11], DALL-E [38], and our FA-VAE model. With a larger compression rate, Figure 6 row 2 shows that more middle and high frequencies are compressed in VQ-GAN and DALL-E. In comparison, FA-VAE can reconstruct middle and high frequencies more accurately, which translates to good representations with improved semantics and local details in Figure 6 row 1. For instance, at a compression rate of 16, the dog’s tongue of

	ablation on	FFL(X, \hat{X})	SL (A_i, C_i)	FCM	kernel $K_i(\mu, \sigma_i)$	DSL (A_i, C_i)	kernel size μ	initial value σ_i	pair-wise σ_i	$\mathcal{L}_1 \downarrow$	$\mathcal{L}_{lpips} \downarrow$	rFID \downarrow
1	VQ-GAN [11]	\times	\times	\times	\times	\times	\times	\times	\times	0.121	0.30	10.12
2	VQ-GAN + Style [53]	\times	\times	\times	\times	\times	\times	\times	\times	0.085	0.23	11.90
3	VQ-GAN [15]	\checkmark	\times	\times	\times	\times	\times	\times	\times	0.114	0.35	30.65
4	SL w/o kernel	\checkmark	\times	CONV	\times	\times	\times	\times	\times	0.082	0.22	7.04
5		\checkmark	\checkmark	CONV	\times	\times	\times	\times	\times	0.082	0.22	7.02
6	SL w/ kernel	\checkmark	\checkmark	CONV	\checkmark	\times	9	3	\times	0.080	0.22	7.39
7	FCM architecture	\checkmark	\checkmark	CONV	\checkmark	\checkmark	9	3	\times	0.081	0.21	5.90
8		\checkmark	\checkmark	RES	\checkmark	\checkmark	9	3	\times	0.078	0.21	6.44
9		\checkmark	\checkmark	ATTN	\checkmark	\checkmark	9	3	\times	0.089	0.23	7.49
10	DSL kernel size μ	\checkmark	\checkmark	RES	\checkmark	\checkmark	3	3	\checkmark	0.081	0.21	6.66
11		\checkmark	\checkmark	RES	\checkmark	\checkmark	5	3	\checkmark	0.081	0.21	7.04
12		\checkmark	\checkmark	RES	\checkmark	\checkmark	9	3	\checkmark	0.082	0.22	6.53
13		\checkmark	\checkmark	RES	\checkmark	\checkmark	11	3	\checkmark	0.083	0.22	7.48
14		\checkmark	\checkmark	RES	\checkmark	\checkmark	15	3	\checkmark	0.083	0.22	6.36

Table 2. Ablation studies on the CelebA-HQ validation dataset [17], visualizations are in Figure 7. Words put in bold to highlight the changing component.

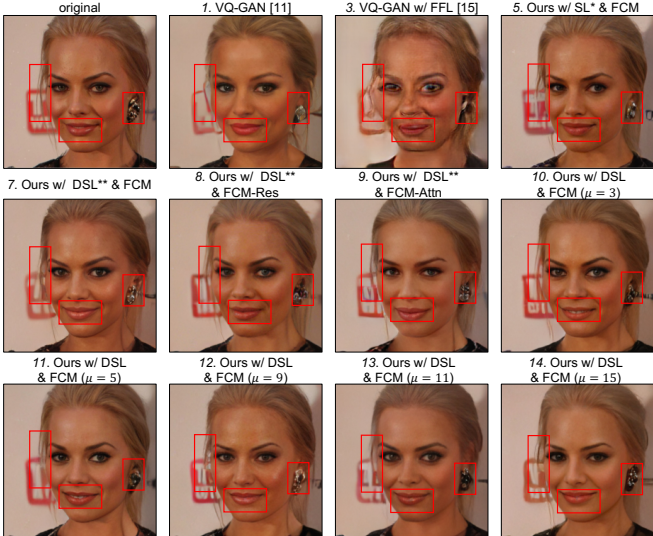


Figure 7. Reconstruction comparisons for ablation studies on CelebA-HQ. The figure number represents the setting in the corresponding row in Table 2. SL* is SL without Gaussian kernel, DSL** is DSL with non pairwise σ . FCM is convolution architecture by default.

FA-VAE’s reconstruction is more similar to the original image than VQ-GAN in terms of color and shape; more qualitative results are in the supplement.

Ablation Studies on FCM and DSL In Table 2, we perform ablation studies on different architectures of FCM in combination with different settings of the Spectrum Loss (SL) and Dynamic Spectrum Loss (DSL). Figure 7 gives the accompanying visualizations of the quantitative results.

First, as motivated in the Section 3, Table 2 row 3 shows that considering all frequencies as equally important leads the VQ-GAN model to poor performance in terms of rFID and lpips (see Figure 7 image 3). In comparison, results in Table 2 rows 4 demonstrate that FCMs alone can help

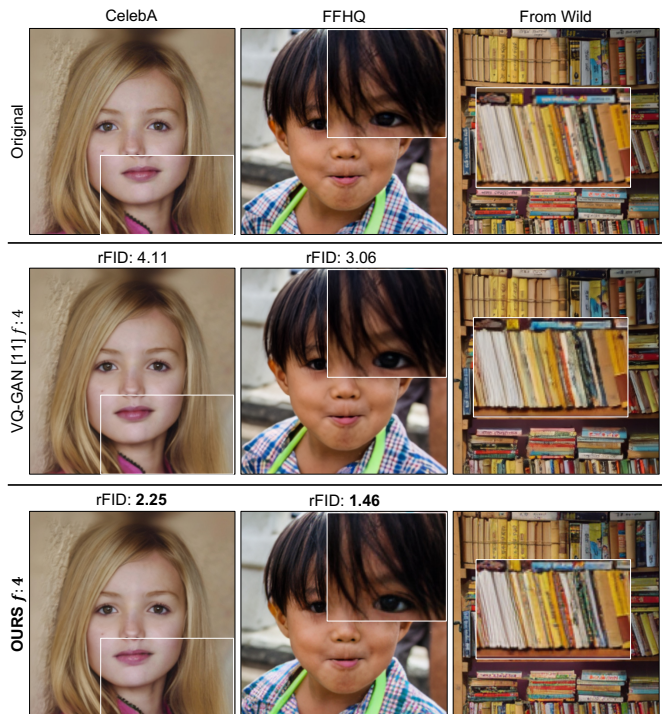


Figure 8. Zero-shot reconstruction on CelebA-HQ [17], FFHQ [21] and photos from the wild, taken from [11]. The models are trained on ImageNet on different compression rates.

FA-VAE model achieve a better reconstruction because the residual connections in FCMs preserve better the information flow. The reconstruction is further improved when combined with a simple SL on images level (row 5) or blocks level (row 6). Although SL (row 6) shows slightly inferior reconstruction due to neglection of frequency importance variance across decoder blocks, Figure 7 image 5 shows that the details, such as earrings and hairs, can still be more enhanced than the baseline model shown in image 1.

the woman has high cheekbones, wavy hair, big nose, mouth open, big lips, pointy nose, and arched eyebrows, she is young and wears heavy makeup, and lipstick.



He has goatee and wears necktie.



Figure 9. Text-to-Image generation on CelebA-HQ-MM [17]

Then, Table 2 rows 7-9 compare the performance when the architecture of FCM varies as illustrated in Figure 5; note that instead of using same σ_i for $(\mathcal{A}_i, \mathcal{C}_i)$, we use two learnable σ for \mathcal{A}_i and \mathcal{C}_i respectively. Quantitatively, when everything else is held equal, the convolution architecture shows better reconstruction than residual and attention architectures. Similarly, Figure 7 image 7 resembles the original image more than images 8 and 9 in terms of face radiance, smoothness, lip color, and shape. The reason is that residual connection enriches the outputs of FCM, which defies the purpose of enriching features of higher frequencies of the decoder features motivated in section 3.1.1. The attention mechanism is at a disadvantage here because the decoder and the encoder exclusively use convolutions.

Finally, varying the size of kernels in DSL (Table 2 row 10 - 14) show quite similar quantitative reconstruction performance, while qualitatively, Figure 7 shows that a larger kernel size tends to produce smoother reconstructions. One reason could be that a larger kernel size tends to smooth more the feature maps because more surrounding values are used during convolution. Thus, in other experiments, we choose a kernel size of 3, and the effects of kernel sizes are open to future works.

Zero-shot Reconstruction To further demonstrate the reconstruction capabilities of FA-VAE models, Table 3 gives the zero-shot reconstruction performance evaluated on CelebA-HQ [17] and FFHQ [21] using models trained on ImageNet [9]. The accompanying qualitative results are in Figure 8. Overall, FA-VAE displays impressive transferability capability with more faithful reconstruction in details, for instance, the light contrast in column 1 and book details in column 3. Note also that the common metric used in image compression PSNR is not perfectly correlated with rFID, but we put the metric here for reference.

4.3. Image Synthesis

Table 4 shows the text-to-image generation performance on CelebA-HQ-MM [17]. Our proposed autoregressive transformer CAT yields a better generation quality than other GAN-based models, including AttnGAN [52], ControlGAN [26], which are solely designed for image generation. Figure 9 shows that CAT can generate satisfactory images conditioned on text inputs of varying lengths. At-

Pretrained Model	f	CelebA		FFHQ	
		rFID \downarrow	PSNR \uparrow	rFID \downarrow	PSNR \uparrow
VQ-GAN [40]	16	8.62	23.40	6.83	22.68
VQ-GAN [11]	4	4.11	31.20	3.06	30.82
FA-VAE (Ours)	16	6.52	22.59	6.19	21.95
FA-VAE (Ours)	4	2.25	31.39	1.46	30.85

Table 3. Zero-shot reconstruction results on the validation data of FFHQ [21] and CelebA-HQ [17] using models trained on ImageNet [9]. f is the downsampling factor, the codebook sizes for $f = \{16, 8, 4\}$ are $\{16384, 16384, 8192\}$ respectively.

Model	FID \downarrow
AttnGAN [52]	125.98
ControlGAN [26]	116.32
DM-GAN [55]	131.05
DF-GAN [44]	137.60
TediGAN [50]	106.37
LAFITE [54]	12.54
CAT (Ours)	10.23

Table 4. Text-to-image generation on CelebA-HQ MM [50].
tributes such as “mouth open” and “arched eyebrows” are captured during generation because all the tokens embeddings are used as a condition which gives more precise guidance. More quantitative and qualitative results on different datasets are in the supplement.

5. Conclusion

In this paper, we introduce the Frequency Augmented VAE (FA-VAE) model, which aims to improve reconstruction quality by bridging the gaps in the frequency domains between original and reconstructed images. New modules named Frequency Complement Modules (FCM) are crafted and guided under the new (Dynamic) Spectrum Loss ((D)SL) to learn to complement the reconstructed features of missing frequencies. A new Cross-attention Autoregressive Transformer (CAT) is proposed for achieving more precise textual-image alignment in the text-to-image generation task. FA-VAE shows improved reconstruction on various datasets compared to SOTA methods.

Acknowledgement

This research is supported in part by the National Science Foundation under award No. 2040209.

References

- [1] Jyoti Aneja, Alexander G. Schwing, Jan Kautz, and Arash Vahdat. Ncp-vae: Variational autoencoders with noise contrastive priors. *ArXiv*, abs/2010.02917, 2020. [2](#)
- [2] Valerio Biscione and Jeffrey S. Bowers. Convolutional neural networks are not invariant to translation, but they can learn to be. *JMLR*, 2022. [5](#)
- [3] Andrew Brock, Jeff Donahue, and Karen Simonyan. Large scale GAN training for high fidelity natural image synthesis. In *ICLR*, 2019. [2](#)
- [4] Huiwen Chang, Han Zhang, Lu Jiang, Ce Liu, and William T. Freeman. Maskgit: Masked generative image transformer. In *CVPR*, 2022. [1](#)
- [5] Ting Chen, Ruixiang Zhang, and Geoffrey Hinton. Analog bits: Generating discrete data using diffusion models with self-conditioning, 2022. [3](#)
- [6] Rewon Child. Very deep {vae}s generalize autoregressive models and can outperform them on images. In *ICLR*, 2021. [1, 2](#)
- [7] Jooyoung Choi, Jungbeom Lee, Chaehun Shin, Sungwon Kim, Hyunwoo Kim, and Sungroh Yoon. Perception prioritized training of diffusion models. In *CVPR*, 2022. [3](#)
- [8] Katherine Crowson, Stella Rose Biderman, Daniel Kornis, Dashiell Stander, Eric Hallahan, Louis Castricato, and Edward Raff. Vqgan-clip: Open domain image generation and editing with natural language guidance. In *ECCV*, 2022. [2, 3, 6](#)
- [9] Jia Deng, Wei Dong, Richard Socher, Li-Jia Li, Kai Li, and Li Fei-Fei. Imagenet: A large-scale hierarchical image database. In *CVPR*, 2009. [6, 8](#)
- [10] Prafulla Dhariwal and Alexander Nichol. Diffusion models beat gans on image synthesis. In *NeurIPS*, 2021. [3](#)
- [11] Patrick Esser, Robin Rombach, and Björn Ommer. Taming transformers for high-resolution image synthesis. In *CVPR*, 2021. [1, 2, 3, 4, 5, 6, 7, 8](#)
- [12] Ge Gao, Pei You, Rong Pan, Shunyuan Han, Yuanyuan Zhang, Yuchao Dai, and Hojae Lee. Neural image compression via attentional multi-scale back projection and frequency decomposition. In *ICCV*, 2021. [2](#)
- [13] Karol Gregor, Ivo Danihelka, Andriy Mnih, Charles Blundell, and Daan Wierstra. Deep autoregressive networks. In *ICML*, 2014. [2](#)
- [14] Martin Heusel, Hubert Ramsauer, Thomas Unterthiner, Bernhard Nessler, and Sepp Hochreiter. Gans trained by a two time-scale update rule converge to a local nash equilibrium. In *NeurIPS*, 2017. [1](#)
- [15] Liming Jiang, Bo Dai, Wayne Wu, and Chen Change Loy. Focal frequency loss for image reconstruction and synthesis. In *ICCV*, 2021. [2, 4, 7](#)
- [16] Justin Johnson, Alexandre Alahi, and Li Fei-Fei. Perceptual losses for real-time style transfer and super-resolution. In *ECCV*, 2016. [1, 2](#)
- [17] Tero Karras, Timo Aila, Samuli Laine, and Jaakko Lehtinen. Progressive growing of gans for improved quality, stability, and variation. *CoRR*, abs/1710.10196, 2017. [7, 8](#)
- [18] Tero Karras, Timo Aila, Samuli Laine, and Jaakko Lehtinen. Progressive growing of GANs for improved quality, stability, and variation. In *ICLR*, 2018. [2](#)
- [19] Tero Karras, Miika Aittala, Janne Hellsten, Samuli Laine, Jaakko Lehtinen, and Timo Aila. Training generative adversarial networks with limited data. In *NeurIPS*, 2020. [2](#)
- [20] Tero Karras, Miika Aittala, Samuli Laine, Erik Häkkinen, Janne Hellsten, Jaakko Lehtinen, and Timo Aila. Alias-free generative adversarial networks. In *NeurIPS*, 2021. [2](#)
- [21] Tero Karras, Samuli Laine, and Timo Aila. A style-based generator architecture for generative adversarial networks. In *CVPR*, 2019. [2, 6, 7, 8](#)
- [22] Soo Ye Kim, Kfir Aberman, Nori Kanazawa, Rahul Garg, Neal Wadhwa, Huiwen Chang, Nikhil Karnad, Munchurl Kim, and Orly Liba. Zoom-to-inpaint: Image inpainting with high frequency details. In *CVPRW*, 2022. [1](#)
- [23] Diederik P Kingma and Max Welling. Auto-encoding variational bayes, 2013. [2](#)
- [24] Umut Kocasari, Alara Dirik, Mert Tiftikci, and Pinar Ynardag. Stylemc: Multi-channel based fast text-guided image generation and manipulation. *2022 IEEE/CVF Winter Conference on Applications of Computer Vision (WACV)*, pages 3441–3450, 2022. [2](#)
- [25] Doyup Lee, Chiheon Kim, Saehoon Kim, Minsu Cho, and Wook-Shin Han. Autoregressive image generation using residual quantization. In *CVPR*, 2022. [1, 2, 3, 4, 6](#)
- [26] Bowen Li, Xiaojuan Qi, Thomas Lukasiewicz, and Philip H. S. Torr. Controllable text-to-image generation. In *NeurIPS*, 2019. [8](#)
- [27] Alex Nichol, Prafulla Dhariwal, Aditya Ramesh, Pranav Shyam, Pamela Mishkin, Bob McGrew, Ilya Sutskever, and Mark Chen. GLIDE: towards photorealistic image generation and editing with text-guided diffusion models. In *ICML*, 2022. [2, 3](#)
- [28] Alexander Quinn Nichol and Prafulla Dhariwal. Improved denoising diffusion probabilistic models. In *ICML*, 2021. [3](#)
- [29] Gaurav Parmar, Dacheng Li, Kwonjoon Lee, and Zhuowen Tu. Dual contradistinctive generative autoencoder. In *CVPR*, 2021. [1, 2](#)
- [30] Yash Patel, Srikanth Appalaraju, and R. Manmatha. Deep perceptual compression, 2019. [5](#)
- [31] Jialun Peng, Dong Liu, Songcen Xu, and Houqiang Li. Generating diverse structure for image inpainting with hierarchical vq-vae. In *CVPR*, 2021. [1](#)
- [32] Stanislav Pidhorskyi, Donald A. Adjeroh, and Gianfranco Doretto. Adversarial latent autoencoders. In *CVPR*, 2020. [2](#)
- [33] Alec Radford, Jong Wook Kim, Chris Hallacy, Aditya Ramesh, Gabriel Goh, Sandhini Agarwal, Girish Sastry, Amanda Askell, Pamela Mishkin, Jack Clark, Gretchen Krueger, and Ilya Sutskever. Learning transferable visual models from natural language supervision. In *ICML*, 2021. [2, 3, 6](#)
- [34] Alec Radford, Jeff Wu, Rewon Child, David Luan, Dario Amodei, and Ilya Sutskever. Language models are unsupervised multitask learners. 2019. [6](#)

[35] Colin Raffel, Noam Shazeer, Adam Roberts, Katherine Lee, Sharan Narang, Michael Matena, Yanqi Zhou, Wei Li, and Peter J. Liu. Exploring the limits of transfer learning with a unified text-to-text transformer. *JMLR*, 21(140):1–67, 2020. [3](#)

[36] Nasim Rahaman, Aristide Baratin, Devansh Arpit, Felix Dräxler, Min Lin, Fred A. Hamprecht, Yoshua Bengio, and Aaron C. Courville. On the spectral bias of neural networks. In *ICML*, 2019. [1](#)

[37] Aditya Ramesh, Prafulla Dhariwal, Alex Nichol, Casey Chu, and Mark Chen. Hierarchical text-conditional image generation with clip latents. *ArXiv*, abs/2204.06125, 2022. [3](#)

[38] Aditya Ramesh, Mikhail Pavlov, Gabriel Goh, Scott Gray, Chelsea Voss, Alec Radford, Mark Chen, and Ilya Sutskever. Zero-shot text-to-image generation. In *ICML*, 2021. [3, 6](#)

[39] Ali Razavi, Aaron van den Oord, and Oriol Vinyals. Generating diverse high-fidelity images with vq-vae-2. In *NeurIPS*, 2019. [1, 2, 3, 6](#)

[40] Robin Rombach, Andreas Blattmann, Dominik Lorenz, Patrick Esser, and Björn Ommer. High-resolution image synthesis with latent diffusion models. In *CVPR*, 2022. [1, 3, 6, 8](#)

[41] Chitwan Saharia, William Chan, Saurabh Saxena, Lala Li, Jay Whang, Emily L. Denton, Seyed Kamyar Seyed Ghasemipour, Burcu Karagol Ayan, Seyedeh Sara Mahdavi, Raphael Gontijo Lopes, Tim Salimans, Jonathan Ho, David J. Fleet, and Mohammad Norouzi. Photorealistic text-to-image diffusion models with deep language understanding. *ArXiv*, abs/2205.11487, 2022. [3](#)

[42] Edgar Schonfeld, Bernt Schiele, and Anna Khoreva. A u-net based discriminator for generative adversarial networks. In *CVPR*, 2020. [2](#)

[43] Jianxin Sun, Qiyao Deng, Qi Li, Muyi Sun, Min Ren, and Zhenan Sun. Anyface: Free-style text-to-face synthesis and manipulation. In *CVPR*, 2022. [2](#)

[44] Ming Tao, Hao Tang, Fei Wu, Xiao-Yuan Jing, Bing-Kun Bao, and Changsheng Xu. Df-gan: A simple and effective baseline for text-to-image synthesis. In *CVPR*, 2022. [2, 8](#)

[45] Arash Vahdat and Jan Kautz. NVAE: A deep hierarchical variational autoencoder. In *NeurIPS*, 2020. [2](#)

[46] Aaron van den Oord, Oriol Vinyals, and koray kavukcuoglu. Neural discrete representation learning. In *NeurIPS*, 2017. [1, 2, 3, 4, 5, 6](#)

[47] Ashish Vaswani, Noam Shazeer, Niki Parmar, Jakob Uszkoreit, Llion Jones, Aidan N Gomez, Łukasz Kaiser, and Illia Polosukhin. Attention is all you need. In *NeurIPS*, 2017. [6](#)

[48] Haohan Wang, Xindi Wu, Zeyi Huang, and Eric P. Xing. High-frequency component helps explain the generalization of convolutional neural networks. In *CVPR*, 2020. [2](#)

[49] Zihao Wang, Wei Liu, Qian He, Xinglong Wu, and Zili Yi. Clip-gen: Language-free training of a text-to-image generator with clip. *arXiv preprint arXiv:2203.00386*, 2022. [1, 2, 3, 6](#)

[50] Weihao Xia, Yujiu Yang, Jing-Hao Xue, and Baoyuan Wu. Tedigan: Text-guided diverse face image generation and manipulation. In *CVPR*, 2021. [2, 6, 8](#)

[51] Zhisheng Xiao, Karsten Kreis, Jan Kautz, and Arash Vahdat. Vaebm: A symbiosis between variational autoencoders and energy-based models. In *ICLR*, 2021. [2](#)

[52] Tao Xu, Pengchuan Zhang, Qiuyuan Huang, Han Zhang, Zhe Gan, Xiaolei Huang, and Xiaodong He. Attngan: Fine-grained text to image generation with attentional generative adversarial networks. In *CVPR*, 2018. [2, 8](#)

[53] Jiahui Yu, Xin Li, Jing Yu Koh, Han Zhang, Ruoming Pang, James Qin, Alexander Ku, Yuanzhong Xu, Jason Baldridge, and Yonghui Wu. Vector-quantized image modeling with improved VQGAN. In *ICLR*, 2022. [5, 7](#)

[54] Yufan Zhou, Ruiyi Zhang, Changyou Chen, Chunyuan Li, Chris Tensmeyer, Tong Yu, Jiuxiang Gu, Jinhui Xu, and Tong Sun. Lafite: Towards language-free training for text-to-image generation. *CVPR*, 2022. [2, 8](#)

[55] Minfeng Zhu, Pingbo Pan, Wei Chen, and Yi Yang. Dm-gan: Dynamic memory generative adversarial networks for text-to-image synthesis. In *CVPR*, 2019. [2, 8](#)